Title

Rapid in vivo apparent diffusion coefficient mapping of hyperpolarized 13C metabolites

Journal

Magnetic Resonance in Medicine, 74(3)

ISSN

0740-3194

Authors

Koelsch, Bertram L

Reed, Galen D

Keshari, Kayvan R

et al.

Publication Date

2015-09-01

DOI

10.1002/mrm.25422

Peer reviewed

HHS Public Access

Author manuscript

Magn Reson Med. Author manuscript; available in PMC 2016 September 01.

Published in final edited form as:

Magn Reson Med. 2015 September ; 74(3): 622–633. doi:10.1002/mrm.25422.

Rapid in vivo ADC Mapping of Hyperpolarized ^{13}C Metabolites

Bertram L. Koelsch[#1,2], **Galen D. Reed**[#1,2], **Kayvan R. Keshari**[3], **Myriam M. Chaumeil**[1], **Robert Bok**[1], **Sabrina M. Ronen**[1,2], **Daniel B. Vigneron**[1,2], **John Kurhanewicz**[#1,2], and **Peder E. Z. Larson**[#1,2]

[1]Department of Radiology and Biomedical Imaging, University of California, San Francisco, California, USA

[2]UC Berkeley – UCSF Graduate Program in Bioengineering, University of California, Berkeley and University of California, San Francisco, California, USA

[3]Department of Radiology and Molecular Pharmacology and Chemistry Program, Memorial Sloan Kettering Cancer Center, New York, USA

[#] These authors contributed equally to this work.

Abstract

Purpose—Hyperpolarized ^{13}C MR allows for the study of real-time metabolism in vivo, including significant hyperpolarized ^{13}C lactate production in many tumors. Other studies have shown that aggressive and highly metastatic tumors rapidly transport lactate out of cells. Thus, the ability to not only measure the production of hyperpolarized ^{13}C lactate but also understand its compartmentalization using diffusion weighted MR will provide unique information for improved tumor characterization.

Methods—We used a bipolar pulsed-gradient double spin echo EPI sequence to rapidly generate diffusion-weighted images of hyperpolarized ^{13}C metabolites. Our methodology included a simultaneously acquired B_1 map to improve apparent diffusion coefficient (ADC) accuracy and a diffusion compensated variable flip angle scheme to improve ADC precision.

Results—We validated this sequence and methodology in hyperpolarized ^{13}C phantoms. Next, we generated ADC maps of several hyperpolarized ^{13}C metabolites in a normal rat, rat brain tumor model, and prostate cancer mouse model using both pre-clinical and clinical trial-ready hardware.

Conclusion—ADC maps of hyperpolarized ^{13}C metabolites provide information about the localization of these molecules in the tissue microenvironment. The methodology presented here allows for further studies to investigate ADC changes due to disease state that may provide unique information about cancer aggressiveness and metastatic potential.

Keywords

hyperpolarized ^{13}C; ADC mapping; diffusion weighted imaging; dissolution DNP; metabolic imaging

Corresponding author: Peder E. Z. Larson, Ph.D. Byers Hall, Room 102C 1700 4th Street San Francisco, CA 94158 peder.larson@ucsf.edu.

Introduction

Fast diffusion weighted (DW) echo-planar imaging (EPI) techniques have allowed apparent diffusion coefficient (ADC) maps of water to become an invaluable tool for the identification and characterization of various cancers (1), including brain tumors (2) and prostate cancer (3). Structural changes in the tissue microstructure caused by the tumor masses alter the local mobility of water molecules and thereby generate contrast in DW images and ADC maps.

The growing field of hyperpolarized ^{13}C magnetic resonance (MR) (4,5) has also proven to be useful in identifying and characterizing tumors by measuring the real-time metabolism of hyperpolarized ^{13}C pyruvate to lactate, in both brain tumors (6) and prostate cancer (7). These abnormally high levels of hyperpolarized ^{13}C lactate arise from a shift towards increased aerobic glycolytic metabolism, a process known as the Warburg effect (8). Currently, in vivo MR studies spatially localize these hyperpolarized ^{13}C metabolites to identify tumor masses (9). However, these acquisitions give no discrimination of the distribution of the hyperpolarized ^{13}C metabolites within the tissue microstructure based on their local mobility.

Having the ability to identify both the overall production of hyperpolarized ^{13}C lactate and its extra- and intracellular distribution could be useful for improved tumor identification and characterization. Research has shown that aggressive and metastatic tumors acidify their extracellular environment (10), a process that facilitates the tumor's invasion into surrounding tissue. Acidification in part happens *via* the export of protons through monocarboxylate transporters (MCTs), which is coupled to the export of lactate (11). Correspondingly, a recent study comparing two renal cell carcinoma cell lines showed that while increased hyperpolarized ^{13}C lactate production was seen in all cancer cell lines, the highly aggressive metastatic cells also rapidly pumped more hyperpolarized ^{13}C lactate out of the cell (12).

Recently, several studies have combined DW techniques with hyperpolarized ^{13}C to rapidly measure the translational motion of these molecules. Solution state studies verified the accuracy of the measurements with diffusion coefficient measurements of molecules with varying molecular weights (13). Cell studies rapidly measuring the ADCs of hyperpolarized ^{13}C pyruvate and lactate have shown that intracellular metabolites have lower diffusion coefficients than the extracellular metabolites (14,15). Animal studies using DW spectroscopic techniques of hyperpolarized ^{13}C metabolites showed improved tumor contrast (16), assessed their vascular and tissue distribution (17) and measured their ADCs in muscle tissue (18). One recent hyperpolarized ^{13}C imaging study used bipolar gradients to suppress flowing vascular spins, which improved metabolic measurements (19). Clinical translation of DW MR of hyperpolarized ^{13}C metabolites will allow for the identification and characterization of tumors based on both the conversion of hyperpolarized ^{13}C pyruvate to lactate and on their localization to various microenvironments.

In this work, we present a technique for rapidly generating ADC maps of hyperpolarized ^{13}C metabolites using a bipolar pulsed-gradient double spin echo, single-shot EPI sequence. The bipolar diffusion gradient pairs produce diffusion weighting (*b*-values) upwards of 1,000 s mm^{-2}, compensating for the relatively small gyromagnetic ration of ^{13}C (γ = 10 MHz T^{-1}) and the limited maximum gradient amplitudes on clinical MR scanners (e.g., 40 mT m^{-1}). Our technique includes a simultaneously generated B_1 map to improve the accuracy of the ADC measurements, while a diffusion compensated variable flip angle (VFA) scheme improves their precision. The technique presented here lays the foundation for generating robust ADC maps of hyperpolarized ^{13}C metabolites on clinical MR scanners and its use in improved characterization of cancers in patients.

Methods

Scanner Hardware

All scans were done on a General Electric Signa MR 3T scanner equipped with a broadband RF amplifier and gradients with 40 mT m^{-1} peak amplitudes and 150 mT m^{-1} ms^{-1} peak slew rates. A custom designed $^{13}C/^{1}H$ dual-tuned transmit/receive birdcage coil was used for mouse studies, rat brain studies and phantom studies; diameter = 5 cm, length = 8 cm, operating in quadrature for both ^{13}C and ^{1}H (20). Whole body rat studies were performed using clinical hardware; a custom designed ^{13}C transmit clamshell coil with two linear 4-channel carbon-tuned receive panels, where each rectangular coil element is 5 × 10 cm (21).

Hyperpolarization

Sample preparation and polarization methods are similar to those previously published (4,22,23). The [1-^{13}C] pyruvate preparation contained neat pyruvic acid, 16.5 mM of the trityl radical OX063 (GE Healthcare) and 1.5 mM Dotarem (Guerbet). The [1-^{13}C] lactate preparation contained equal parts glycerol and a 50% by weight solution of sodium [1-^{13}C] lactate, 15mM of the trityl radical and 1 mM Dotarem. HMCP (bis-1,1-(hydroxymethyl)-[1-^{13}C]cyclopropane-d_8), also referred to as HP001, was mixed with water in a ratio of 2.78:1 by weight, with 19 mM OX063 and 1.2 mM Dotarem. A HyperSense (Oxford Instruments) was used for dynamic nuclear polarization (DNP), operating at 3.35 T, 1.3 K and 94.100 GHz microwave irradiation for a minimum of 45 min. After polarization, pyruvate was dissolved with an 80 – 100 mM NaOH saline solution with 10mM TRIS to achieve 80 mM (for mice) or 100 mM (for rats) solutions of hyperpolarized [1-^{13}C] pyruvate at pH ≈ 7.4. Lactate and HMCP were dissolved with a phosphate-buffered saline solution at 40 mM and 100 mM concentrations, respectively, at pH ≈ 7.4.

^{1}H Diffusion Imaging

DW proton images were acquired with a pulsed gradient single spin echo sequence. These images were acquired in the axial plane and diffusion weighting was applied in the through-slice direction at *b*-values = [0, 600] s mm^{-2}, echo time (TE) = 68 ms, repetition time (TR) = 4 s, 1.25×1.25 mm resolution, 64×64 matrix, 4 mm slice thickness, 16 averages.

Hyperpolarized ^{13}C Diffusion Imaging

Prior to hyperpolarized ^{13}C studies, rough flip angle calibrations were performed by measuring the transmitter power required to produce a signal null ($\theta = 180°$) with a thermally polarized 8 M ^{13}C urea phantom, doped with 2 mM Dotarem, placed at the edge of the coil. Hyperpolarized ^{13}C DW imaging experiments were performed using a bipolar pulsed-gradient double spin echo sequence with a single-shot flyback EPI readout; total readout time = 32.6 ms, echo spacing = 2.9 ms, duty cycle = 41.4% (Figure 1). Similar to prior ^{13}C spin echo acquisitions (13,17,24,25), the sequence consisted of a slice-selective excitation pulse followed with a pair of adiabatic refocusing pulses.

A symmetric-frequency response, “true null” spectral spatial pulse (26) was designed similar to those used in prior hyperpolarized ^{13}C studies to excite a single metabolite (27,28). This excitation had a 60 Hz full-width half-maximum (FWHM) spectral bandwidth, 13 mm minimum slice thickness, 400 Hz stop-band, and was designed to alternatively excite [1-^{13}C] lactate and [1-^{13}C] pyruvate, which have a 390 Hz chemical shift separation at 3.0 T.

The dual-tuned ^{13}C/^{1}H dual-tuned transmit/receive birdcage coil used 10 ms sech/tanh (HS*n*, *n*=1) adiabatic 180° refocusing pulses (25); refocusing bandwidth = 2000 Hz and peak-power at adiabatic threshold = 1 G. The ^{13}C transmit clamshell coil used low-power 15 ms stretched hyperbolic secant (HS*n*, *n*=3) adiabatic 180° refocusing pulses (29,30); refocusing bandwidth = 600 Hz and peak-power at adiabatic threshold = 0.3 G. Both adiabatic pulses were nominally run at 20% above the adiabatic threshold. RF and gradient spoiling were used to ensure transverse magnetization would not carry-over to subsequent scans.

Bipolar diffusion gradients pairs surrounding each of the refocusing pulses (31) maximized the diffusion-sensitizing period and thereby considerably increased the diffusion weighting achievable with this sequence; *b*-values up to 1,000 s mm^{-2} for ^{13}C with the parameters used in these studies. All diffusion gradients were applied in the through slice direction. To vary the diffusion weighting between scans, only the gradient amplitudes were changed (0 – 40 mT m^{-1}), while diffusion gradient durations (22 ms each) and TE were kept constant to eliminate T_2-weighting differences between scans. The diffusion weighting between scans were changed as a function of the maximum *b*-value, i.e. *b*-values = b_{max}·[1, 0.3125, 0.01, 0.01]. Each hyperpolarized ^{13}C molecule was scanned four times within a 1 s total acquisition time (Figure 2); TE=175 or 180 ms, TR=250 ms. For the experiments where both hyperpolarized ^{13}C pyruvate and lactate were imaged, the latter was image first.

Variable Flip Angle Schemes

All acquisitions made use of a variable flip angle (VFA) scheme that was designed to consume the entire pool of the non-renewable hyperpolarized signal. Unless mentioned otherwise, the flip angles were changed between scans according a standard VFA scheme, $\theta_n = arctan\left(1/\sqrt{N-n}\right)$ (32,33). For four scans (N = 4), the flip angles were 30°, 35°, 45° and 90°. In the absence of diffusion gradients and flip angle inaccuracies, all four images

have comparable signal-to-noise (SNR). The application of diffusion gradients results in scan-specific signal loss proportional to the *b*-value applied.

A diffusion compensated VFA scheme was designed to improve ADC measurement precision by increasing the SNR at higher *b*-value images. Signal loss due to diffusion weighting for a given diffusion coefficient and *b*-value scheme was compensated for with increased flip angles, producing constant SNR across all DW images for all signal with this diffusion coefficient. Here, the $D = 0.83 \times 10^{-3}$ mm^2 s^{-1} and $b_{max} = 1005$ s mm^{-2} give the flip angles 50°, 42°, 45° and 90°.

In all VFA schemes, the effect of longitudinal T_1 relaxation was neglected given that the total scan time (1 s) was much less than T_1 for the hyperpolarized ^{13}C molecules.

Phantom Experiments

Upon dissolution from the HyperSense, 1 mL of the hyperpolarized compound was thoroughly mixed with 59 mL of room temperature, deionized water. The final temperature of this solution was 22°C ± 1, as measured with an infrared thermometer. The thoroughly mixed solution was added to a 60 mL syringe and placed into the coil within the scanner. The solution was allowed to settle for 90 s before scanning to minimize non-diffusive motion. Shorter settling intervals produced non-uniform signal loss with DW imaging, indicative of non-diffusive motion. Phantoms were scanned in the coronal plane at 3.3×3.3 mm resolution, 24×12 matrix and one 13 mm slice.

Animal Experiments

Animal studies were performed under a protocol approved by the UCSF Institutional Animal Care and Utilization Committee. Animals were anesthetized with an isoflurane/oxygen mixture and placed on a pad heated to 37°C. All anatomic images were acquired in axial and coronal planes with a T_2-weighed fast spin echo (FSE), using either the ^{13}C/^{1}H dual-tuned transmit/receive birdcage coils or the MR scanner's body coils. Transgenic prostate cancer mouse models (TRAMP) at different stages of tumor progression were used. Hyperpolarized ^{13}C diffusion images for mice were acquired in the coronal plane at 3.3×3.3 mm resolution, 24×12 matrix, one 50 mm slice with $b_{max} = 969$ or 1005 s mm^{-2}. Hyperpolarized ^{13}C images of brain tumor bearing rats were acquired in the axial plane at 3.3×3.3 mm resolution, 12×12 matrix, one 13 mm slice with $b_{max} = 1005$ s mm^{-2}. These tumors were induced via intracranial injection of U87 glioblastoma cells ($3x10^5$ cells in 10 μL) on in 5 – 6week old athymic rats (34) and were scanned approximately 30 days later. Whole body hyperpolarized ^{13}C diffusion image of normal Sprague Dawley rats, using the custom ^{13}C transmit clamshell coil and receive coil array, were scanned with 8.8×8.8 mm resolution, 24×12 matrix, one 20 mm slice with $b_{max} = 933$ s mm^{-2}. The relatively large slices used in all experiments were implemented to achieve sufficient SNR with diffusion weighting. For experiments using the diffusion compensated VFA scheme, flip angles were 50°, 42°, 45° and 90°. All animals were imaged 35 s after the start of a 12 s injection.

Data Analysis

Proton ADC maps were generated by fitting the signal on a per-voxel basis to the following equation describing the signal response as a function of the diffusion weighting applied (*b*-value):

$$ln\left(S_i/S_0\right) = -\,b \cdot ADC \quad (1)$$

where S_i is the diffusion sensitized signal for a certain *b*, while S_0 is the non-diffusion sensitized signal, and the slope represents the ADC.

The *b*-values for hyperpolarized ^{13}C scans were determined from numerical integration according to (35):

$$b = \gamma^2 \int_0^{TE} k^2\left(t\right) dt \quad (2)$$

where

$$k\left(t\right) = \frac{\gamma}{2\pi} \int_0^t G\left(t'\right) dt' \quad (3)$$

Encoding and readout gradients each produced *b*-values << 1 s mm^{-2} and thus were neglected for all ADC measurements. The shaded area in Figure 1b shows how diffusion weighting is proportional to $|k^2(t)|$.

Creating ADC maps of the hyperpolarized ^{13}C molecules with our methodology was a multistep process, summarized with the schematic in Figure 2. After acquisition, a B_1 map of the sample was created to correct for any errors in the transmit-gain/deviations from the expected flip angle excitations. The final two images were acquired with minimal diffusion weighting, maximizing the sample SNR used to generate the B_1 map. Having acquired these images with 45° and 90° flip angles, we used a modified version of the double angle method (36) that accounts for the non-renewable hyperpolarized magnetization. Using the double angle identity

$$sin\left(2\theta\right) = 2\,sin\left(\theta\right) cos\left(\theta\right) \quad (4)$$

and correcting for use of the non-renewable hyperpolarized magnetization by a factor of cos(θ), we can compare the signal (S) of images of scans 3 and 4

$$\frac{S_4}{S_3} = \frac{2\,sin\left(2\theta_3\right) cos\left(\theta_3\right)}{sin\left(\theta_3\right)} = \frac{2\,sin\left(\theta_3\right) cos\left(\theta_3\right) cos\left(\theta_3\right)}{sin\left(\theta_3\right)} = 2 \quad cos^2\left(\theta_3\right) \quad (5)$$

where solving for θ_3 on a per-voxel basis gives the true flip angle used in scan 3. Comparison with the expected flip angle for scan 3 (45°), gives the error in the flip angles. Performing this calculation on all voxels with SNR > 4 results in the B_1 map. This map was subsequently used to correct flip angle for each scan and the voxel-wise signal for each scan:

$$S_{n,corr}=S_{n,acq}/\left\{sin\ (\theta_n)\cdot\prod_{k=1}^{n-1}cos\ (\theta_k)\right\} \quad (6)$$

The ADC map for each hyperpolarized ^{13}C metabolite was created from the first three images, acquired at three different *b*-values. Note that the VFA schemes are designed for four images, the last two of which are used to create the B_1 map while only the first three images were used for generating the ADC maps. Thus, making the ADC maps does not use all the hyperpolarized magnetization. The ADC values were fit according to equation 1. For quantification, hyperpolarized ^{13}C images, B_1 maps and ADC maps were kept at the acquired resolution. ADCs in the text are presented as mean ± standard deviation for the number voxels (N_{vox}) within a region of interest (ROI). The Mann-Whitney U test for independent observations, which does not require normally distributed data, was used for statistical comparisons of ADCs from different ROIs within the same animal ($\alpha = 0.05$).

Co-registration of ^{1}H and ^{13}C images was done by first interpolating the ^{13}C images to the resolution of the corresponding ^{1}H image. The images were overlaid based on their locations and the ROIs were manually drawn for use in quantification of both the ^{13}C and ^{1}H images. For representation, all hyperpolarized ^{13}C DW images were interpolated, while B_1 and ADC maps were left at the acquired resolution.

Diffusion coefficients of pyruvate and lactate were taken from previously published values (13), adjusted for temperature and viscosity using the Stokes-Einstein equation. The diffusion coefficient for HMCP was measured on an NMR spectrometer at 22°C using a previously published method (13).

T_1 relaxation was neglected from all calculations due to the short TR used. All data analysis was done in Matlab (MathWorks Inc).

Simulations

The effects of transmit-gain/excitation flip angle errors on ADC measurement accuracy were assessed with simulations. Diffusion data for a physiologically relevant range of diffusion coefficients (true ADC = 0.2 – 2.2 × 10^{-3} mm^2 s^{-1}) were simulated for the *b*-values scheme presented in Figure 2 (*b*-values = [969, 303, 9.7, 9.7] s mm^{-2}) with flip angle deviations from the expected flip angles (θ = [30°, 35°, 45°, 90°]) of ± 20%. ADCs were then fit from these data by fitting points 1 – 3 to equation 1. Each measured ADC was compared with the true ADC to quantify the resulting error in ADC measurements as a result of flip angle errors.

As discussed above, a diffusion compensated VFA scheme was designed to counteract signal loss due to diffusion weighting at different *b*-values. The resulting diffusion compensated VFA scheme produces images with relatively constant SNR across all scans and different *b*-values. Specifically, signal from molecules with the ADC used to design the specific diffusion compensated VFA will have constant SNR across all images. Signal from molecules with smaller and larger ADCs will experience a slight decrease and increase in SNR, respectively, across the images acquired with the *b*-value scheme used here. However,

all molecules, regardless of ADC, will have improved SNR at the higher *b*-values with the diffusion compensated VFA than with the standard VFA. To assess how this SNR improvement at higher *b*-values improves ADC measurements, a Monte Carlo simulation was run to compare ADCs measured with the standard VFA scheme (θ = [30°, 35°, 45°, 90°]) and the diffusion compensated VFA scheme (θ = [50°, 42°, 45°, 90°]). Simulated data was generated for three physiologically relevant diffusion coefficients, true ADC = [0.3, 0.8, 1.3] × 10^{-3} mm^2 s^{-1} with *b*-values = [1005, 314, 10, 10] s mm^{-2}. Note that while the diffusion compensated VFA was designed for molecules with D = 0.83 × 10^{-3} mm^2 s^{-1}, simulations were also run on molecules with both smaller and greater ADCs than this D, since this will be the case in vivo. Pseudorandom noise with normal distribution and scaled to a specified SNR for the last low *b*-value scan for the standard VFA scheme was added to all simulated data. The simulated diffusion compensated VFA data was flip angle corrected. All ADCs were calculated using equation 1. The effect of noise was simulated 5,000 times for each of the two VFA schemes. These data are presented as mean ± standard deviation. Levene's test for equality of variances was used to statistically compare the simulated ADC distributions between the standard and the diffusion compensated VFA schemes at each true ADC value and at each specified SNR level (α = 0.05). Levene's test does not require data to be normally distributed, which was seen for the distribution of the simulated ADCs at low SNR. A rejection of the null-hypothesis identifies a difference in the variance of the two simulated ADC datasets. All simulations were done in Matlab (MathWorks, Inc.).

Results Improving ADC Mapping Accuracy and Precision

The bipolar pulsed-gradient double spin echo EPI sequence (Figure 1) with a VFA and *b*-value scheme (Figure 2a) was designed to efficiently generate ADC maps of hyperpolarized ^{13}C metabolites on a clinical MRI scanner. The *b*-values were chosen to probe the distribution of the hyperpolarized ^{13}C signal in different environments: the overall signal at a low *b*-value (≈ 10 s mm^{-2}), the extravascular signal with the mid *b*-value (≈ 300 s mm^{-2}) and the highly restricted signal with a high *b*-value (≈ 1,000 s mm^{-2}). In addition to diffusion weighting, long sequence TEs could also contribute to reduced vascular signal where these ^{13}C molecules have shorter T_2s (17). ADCs were calculated by using all three of these *b*-values.

MRI studies are prone to transmit-gain miscalibrations, resulting in either an over- or underestimation of the prescribed flip angle. Spatial variations in the transmit B_1 field, which can be quite large over humansized volumes, may cause local excitation flip angle offsets. In the case of hyperpolarized experiments, where all scans draw signal from a non-renewable pool of longitudinal magnetization, B_1 errors propagate between scans and lead to quantification inaccuracies. The simulation presented in Figure 3a shows how flip angle errors will skew ADC calculations for hyperpolarized ^{13}C molecules. The magnitude of the error depends on the true ADC of the molecules. For example, the black dotted line represents the true ADC of pyruvate in solution, 0.96 × 10^{-3} mm^2 s^{-1} (13). In this case, a -17% flip angle offset results in 13% ADC overestimation. The use of the VFA makes ADC measurement errors resulting from flip angle offsets dependent on the ordering of the *b*-value, where strategic placement of the different *b*-value scans will minimize these errors. Figure 3a shows the errors resulting from the *b*-value scheme presented in Figure 2a.

Transmit-gain errors can be corrected with a simultaneous acquisition of a B_1 map, allowing for flip angle corrections and improved measurement accuracy. The sequence and B_1 mapping methodology was validated with hyperpolarized ^{13}C pyruvate and lactate phantoms. Using two low *b*-value images maximizes the sample SNR used to create the B_1 map. For hyperpolarized ^{13}C pyruvate, the simultaneously acquired B_1 map (Figure 2b) shows a -17 ± 1% flip angle offset in the center of the image. The B_1 map pattern aligns with our expectations for a birdcage coil, with decreased flip angles at either end of the coil and axially increased flip angles close to the rungs of the coil. Figure 3b shows the ADC distribution per voxel from a centered ROI in the hyperpolarized ^{13}C pyruvate phantom ADC map (Figure 2c) both before (uncorrected) and after (corrected) flip angle correction. The mean ADC shifts 13%, from $1.12 \pm 0.05 \times 10^{-3}$ mm^2 s^{-1} (N_{vox} = 83) to $0.97 \pm 0.05 \times 10^{-3}$ mm^2 s^{-1} (N_{vox} = 83) ($p << 0.05$), where the latter agrees with previous diffusion coefficient measurements of pyruvate, 0.97×10^{-3} mm^2 s^{-1} (13). The ADC measured from a hyperpolarized ^{13}C lactate phantom was $0.92 \pm 0.10 \times 10^{-3}$ mm^2 s^{-1} after the flip angle correction (data not shown), which also agrees with previous measurements, 0.88×10^{-3} mm^2 s^{-1} (13).

VFA schemes have been developed for hyperpolarized molecules to produce a constant signal response and allow for a complete exhaustion of the hyperpolarized magnetization (32,33). DW MR experiments are characterized by signal loss corresponding to increasing *b*-values, which may lead to SNR limited images where noise can skew ADC calculations. To compensate for this effect and improve ADC measurement precision, we have created a diffusion compensated VFA scheme (Figure 4). In essence, for a given *b*-value scheme and an expected ADC, the diffusion compensated VFA scheme will produce images with constant SNR. Here, we used $D = 0.8 \times 10^{-3}$ mm^2 s^{-1} and *b*-values = [1005, 314, 10, 10] s mm^{-2}, resulting in a VFA scheme where θ = [50°, 42°, 45°, 90°]. The Monte Carlo simulation in Figure 4a compares the normalized ADCs for both the standard and the diffusion compensated VFA schemes. Signal from molecules with smaller and larger ADCs than that used to design the specific diffusion compensated VFA scheme (e.g., 0.3×10^{-3} mm^2 s^{-1} and 1.3×10^{-3} mm^2 s^{-1} in Figure 4a) will experience a slight signal decrease or increase, respectively, across the DW images with the given *b*-value scheme. Nevertheless, the diffusion compensated VFA scheme produces higher SNR at the high *b*-value images for these molecules and thereby improves their ADC measurement precision. For the range of physiologically relevant ADCs presented and using the same diffusion compensated VFA scheme, tighter standard deviations show significantly improved measurement precision (*p*-value < 0.05 for all plotted pairs using Levene's test for equality of variances). The greatest improvement in ADC measurement precision is seen at lower SNRs where the effect of noise can considerably skew ADC calculations. Figures 4c and 4d illustrate the SNR in the DW images of hyperpolarized ^{13}C pyruvate and lactate with both the standard and the diffusion compensated VFA schemes. Acquired 1 hour apart, these images are from the same TRAMP mouse that had a small, early stage tumor.

In vivo ADC Mapping in Tumor Models

In vivo comparison of ^{1}H water and hyperpolarized ^{13}C pyruvate and lactate DW images and ADC maps in a brain tumor-bearing rat (Figure 5) shows how each of these may

provide unique information. In general, brain tumors are characterized by increased water ADCs relative to the surrounding normal tissue (37,38). This phenomenon is seen in the water ADC map (Figure 5b) where the mean ADC in the tumor region is $1.28 \pm 0.30 \times 10^{-3}$ mm^2 s^{-1} (N_{vox} = 334), while the surrounding normal brain's ADC is $0.84 \pm 0.18 \times 10^{-3}$ mm^2 s^{-1} (N_{vox} = 847) (p-value < 0.05). Hyperpolarized ^{13}C DW images were acquired with a standard VFA scheme. In comparison to the water ADC map, that of hyperpolarized ^{13}C pyruvate (Figure 5c) does not show significant contrast between the tumor area, $0.60 \pm 0.36 \times 10^{-3}$ mm^2 s^{-1} (N_{vox} = 3), and the surrounding normal brain, $0.71 \pm 0.24 \times 10^{-3}$ mm^2 s^{-1} (N_{vox} = 7) (p-value = 0.83). This may be due to the fact that hyperpolarized ^{13}C pyruvate is injected in large excess relative to how much is taken up by the cell. This means that extracellular hyperpolarized ^{13}C pyruvate components may dominate the ADC measurements. Hyperpolarized ^{13}C lactate (Figure 5d), however, does show a significant ADC decrease in the tumor, $0.17 \pm 0.03 \times 10^{-3}$ mm^2 s^{-1} (N_{vox} = 3), in comparison to the surrounding tissue $0.44 \pm 0.14 \times 10^{-3}$ mm^2 s^{-1} (N_{vox} = 7) (p-value = 0.02). These ADC differences between the normal brain and tumor tissue are indicative of microenvironments in which these molecules reside, suggesting that hyperpolarized ^{13}C lactate resides in a more hindered environment in the tumor relative to normal brain than water. ^{1}H and ^{13}C DW image distortions are due to the single-shot EPI acquisition (39).

Hyperpolarized ^{13}C pyruvate was injected into TRAMP mouse bearing a large prostate tumor. Figure 6 shows the low and high b-values DW images of hyperpolarized ^{13}C lactate, acquired with the standard VFA scheme. The high b-value image clearly shows increased tumor contrast for lactate. Correspondingly, the ADC map shows decreased ADCs in the tumor region, $0.37 \pm 0.09 \times 10^{-3}$ mm^2 s^{-1} (N_{vox} = 8), when compared to the immediately surrounding tissue, $0.79 \pm 0.18 \times 10^{-3}$ mm^2 s^{-1} (N_{vox} = 24) (p-value < 0.05). The middle b-value lactate image and all hyperpolarized ^{13}C pyruvate DW images for this animal were unusable because signal loss due to respiratory motion. Similarly, water DW images were also unusable. Respiratory gating for these DW scans will be essential in future studies in the abdomen.

ADC Mapping on Clinical-Ready Hardware

All experiments discussed henceforth used the $^{13}C/^{1}H$ dual-tuned transmit/receive birdcage coil. The clamshell ^{13}C transmit coil used in the recent clinical trial (9), however, is limited by its peak transmitter power and hence a low bandwidth stretched hyperbolic secant (HS3) refocusing pulse was employed. Figure 7 demonstrates the hyperpolarized ^{13}C DW imaging and ADC mapping methodology developed here on clinical trial ready hardware. We injected a normal rat with hyperpolarized ^{13}C HMCP and used the ^{13}C clamshell transmit coil with the 8-channel array ^{13}C receive coil. To ensure that the adiabatic pulses would fully refocus the transverse magnetization, the transmitter power was intentionally set higher than the adiabatic threshold. This also resulted in over-flipping with the spectral-spatial excitation pulses. While use of the diffusion compensated VFA scheme should produce relatively constant SNR for the acquired DW images, the decreasing DW image SNR with decreasing b-values (Figure 7b) shows the result of using larger than desired excitation pulses. The B_1 map (Figure 7c) confirms this over-excitation and shows a flip angle error of 22 ± 2% across the entire animal, where such a slowly varying distribution is expected for

the clamshell transmit coil. Figure 7d shows the DW images after flip angle correction with the B_1 map. The ADC map of hyperpolarized ^{13}C HMCP (Figure 7e) shows an average tissue ADC of $0.73 \pm 0.08 \times 10^{-3}$ mm^2 s^{-1} (N_{vox} = 70) in the abdominal region. The regions of increased ADC appear in the center of the rat at the descending aorta and in a portion of the intestine on the right. For comparison, the solution ADC of HMCP at 22°C is $0.83 \pm 0.01 \times 10^{-3}$ mm^2 s^{-1}. We expect that HMCP resides only in vasculature and extracellular spaces, where it would have an ADC more similar to that in solution.

Discussion

Challenges of Hyperpolarized ^{13}C ADC Mapping

Several factors limit the generation of quantitatively reliable ADC maps of hyperpolarized ^{13}C molecules on a clinical MR scanner: 1) the small gyromagnetic ratio of ^{13}C, 2) the limited maximum gradient amplitudes, 3) the highly dynamic nature of these signals due to metabolism and flow, 4) the non-renewable hyperpolarized magnetization and 5) the difficulty in accurately calibrating transmit B_1 powers.

The first two limitations can be overcome with the bipolar pulsed-gradient double spin echo sequence (Figure 1) that can produce *b*-values up to 1,000 s mm^{-2}, using 40 mT m^{-1} gradient amplitudes and TE = 175 – 180 ms. The relatively long (0.2 – 1+ s) in vivo T_2s of the ^{13}C nuclei generally used for hyperpolarized studies (17,40,41) allow for the long sequence TEs required in these studies to achieve sufficient diffusion weighting without resulting in significant T_2-weighting.

The third challenge, highly dynamic signals, is overcome by acquiring all diffusion images within a time period that is short relative to T_1, metabolism and flow effects (1 s per metabolite in our methodology), and thereby minimizing signal changes not due to diffusion.

The use of a VFA scheme overcomes the fourth and fifth limitations. By design, the VFA scheme maximizes total scan SNR by utilizing the entire pool of hyperpolarized magnetization over all acquisitions. The final two scans taken at 45° and 90° can be compared with a modified version of the double angle B_1 calibration method to correct for transmit power offsets. This simultaneously acquired B_1 map is subsequently used to flip angle correct the DW images and thereby improved the accuracy of the ADC calculations. With low SNR images, B_1 map accuracy will suffer. But, given that B_1 fields spatially vary slowly, spatial filters can be applied to the images to improve estimation of flip angle errors. Of course, where reliable B_1 maps have been previously measured, acquisition of only one low *b*-value image is necessary and redistribution of the non-renewable hyperpolarized magnetization will increase SNR in the other images. Finally, the diffusion compensated VFA scheme (Figure 4) increases image SNR at high *b*-values and improves the precision of ADC calculations. The optimal diffusion compensated VFA scheme depends on the scan parameters, such as the *b*-values and acquisition ordering, and the ADCs in the system under study.

ADC mapping of hyperpolarized ^{13}C metabolites share several challenges with the hyperpolarized gas field. These include the difficulty in measuring transmit B_1 fields to implement accurate flip angles (42) and the use of a VFA scheme to maximize image SNR of the non-renewable magnetization (32,33). Yet, hyperpolarized gas ADC values are several orders of magnitude greater than those of tissue metabolites, for example ≈ 15 mm^2 s for ^3H in the normal lung (43). Correspondingly, *b*-values are merely 0.6 s mm^{-2} and easily achievable with clinical gradient amplitudes and a simple pulsed gradient diffusion sequence (44).

General Considerations for Hyperpolarized ^{13}C ADC Mapping

ADC mapping of hyperpolarized ^{13}C metabolites provides a means for understanding the local microstructure in which these molecules reside. The differences between the water and the hyperpolarized ^{13}C pyruvate and lactate ADCs in the rat brain tumor model (Figure 5) indicate that these may provide unique information about diseased tissue. Understanding how the ADCs of hyperpolarized ^{13}C metabolites change with tumor progression may prove to have a unique diagnostic value for cancer identification and characterization and monitoring of treatment response. In particular, hyperpolarized ^{13}C lactate distribution between the extra- and intracellular may give information about tumor aggressiveness and metastatic potential, given that many metastatic tumors overexpress MCT4s, which rapidly transport lactate and protons out of the cell (45-47).

The in vivo hyperpolarized ^{13}C pyruvate and lactate values measured here are similar to those previously measured in vivo using hyperpolarized ^{13}C spectroscopy on pre-clinical MR scanners(17,18). Lactate generated from pyruvate had lower ADC values most likely because it has a larger intracellular fraction.

Additionally, the hyperpolarized ^{13}C lactate ADCs in the rat brain tumor ($0.17 \pm 0.03 \times 10^{-3}$ mm^2 s^{-1}) and the TRAMP prostate tumor ($0.37 \pm 0.09 \times 10^{-3}$ mm^2 s^{-1}), acquired in 1 s, are similar to previous ^1H spectroscopy measurements of thermally polarized lactate in tumors, acquired over several minutes: 0.23×10^{-3} mm^2 s^{-1} for steady-state ^1H lactate using a double-quantum coherence-transfer technique (48) and 0.13×10^{-3} mm^2 s^{-1} for [3-^{13}C] lactate using a {^1H-^{13}C} editing technique (49). Differences between the ADC values measured here and those previously published could be due to unaccounted for anisotropic effects, incomplete compensation of non-diffusive signal changes, different tissue structure or higher intra-voxel fractions of extracellular or vascular hyperpolarized ^{13}C lactate. The studies presented here foremost demonstrate the feasibility of rapidly measuring the ADCs of hyperpolarized ^{13}C metabolites in vivo on a clinical scanner. Future studies are required to confirm the reproducibility of these measurements and more fully understand the biological/pathological underpinnings of the observed hyperpolarized ^{13}C lactate ADC changes and how they relate to tumor grade.

ADC maps only show the effect of molecular motion in the directions that diffusion gradients have been applied. Clinically, diffusion gradients are applied in anywhere from 1 to 6 or more directions (3,50), where more directions provide information about anisotropic tissue structure. In the work here, diffusion gradients were only applied in the through slice direction to maximize image SNR with the non-renewable hyperpolarized ^{13}C signal. Future

studies will explore the effects of tissue anisotropy on ADCs of hyperpolarized ^{13}C molecules.

The *b*-values used clinically vary depending on the organ under study. For cancer applications, three *b*-values are recommended: a low *b*-value ≈ 0 s mm^{-2}, a mid *b*-value ≥ 100 s mm^{-2} and a high *b*-value ≥ 500 s mm^{-2} (1). With this in mind, the studies here used three *b*-values in these ranges to generate the ADC maps. Given differences in their distribution, however, the DW signal response of hyperpolarized ^{13}C metabolites may not mirror that of water and depend on whether scans are of the injected hyperpolarized ^{13}C molecule (e.g., pyruvate) or of a molecule that has been generated in cells *via* a metabolic pathway (e.g., lactate). Therefore, further studies must explore the optimal *b*-values needed for measuring hyperpolarized ^{13}C metabolite ADCs.

Many studies have assessed the compartmentalization of molecules in tissue with multi-exponential fitting of the DW signal response, including for water (51) and lactate (49). These approaches generally use *b*-values >> 1,000 s mm^{-2} and bi-exponential fitting to measure fast and slow ADC values, attributed to extra- and intracellular fractions, respectively. Clinically, however, mono-exponential (or log-linear) fitting are most commonly used with high *b*-values ≈ 1,000 s mm^{-2}, as we have done here. In this case, ADCs show whether restricted or unrestricted environments dominate. Along with future studies on determining the optimal *b*-values for DW imaging, multi-exponential fitting will be implemented to explore the multiple diffusion compartments.

Translation to Humans

This study demonstrated that sufficiently high *b*-values can be obtained on a clinical MRI scanner for ADC measurements of hyperpolarized ^{13}C metabolites. Moreover, techniques were developed for improving ADC measurement accuracy and precision using clinical RF coils and low-power pulses suitable for use in humans (Figure 7).

The first human studies using hyperpolarized ^{13}C pyruvate showed the production of hyperpolarized ^{13}C lactate in regions of prostate cancer with a SNR ≈ 5 – 15 (9), which we expect to be improved by several fold with improved polarizer hardware, agent delivery, RF coils and pulse sequences. Acquiring 4 DW images will reduce the individual image SNR by $\sqrt{4}=2$. This would result in hyperpolarized ^{13}C lactate SNRs similar to that observed in these studies when using minimal diffusion weighting (SNR ≈ 8 – 45), which were adequate for ADC quantification. Furthermore, the preliminary animal studies demonstrated significantly different tumor ADCs from surrounding tissues. Taken together, these results suggest that the SNR in humans will be sufficient to measure significantly different hyperpolarized ^{13}C lactate ADCs in tumor regions. The techniques developed here to improve the ADC measurement accuracy and precision will improve the quality and reliability of in human hyperpolarized ^{13}C ADC measurements.

Conclusion

In this study, we discussed a methodology for generating quantitatively reliable ADC maps of hyperpolarized ^{13}C molecules. To our knowledge, these are the first in vivo ADC maps of

hyperpolarized ^{13}C metabolites on a commercial MRI system, which represents the first step towards clinical translation of this technique. To achieve sufficient diffusion weighting for the ^{13}C molecules on a clinical MRI scanner, we employed a bipolar pulsed-gradient double spin echo sequence, generating *b*-values upwards of 1,000 s mm^{-2} on a clinical MR scanner. ADC accuracy was improved with flip angle correction based on a simultaneously acquired B_1 map. ADC precision was improved with a diffusion compensated VFA scheme. Here we studied the ADCs of hyperpolarized ^{13}C pyruvate, lactate and HMCP in vivo. ADC changes in these metabolites gives an indication of their microenvironment. In the case of hyperpolarized ^{13}C lactate, ADC changes may provide useful information for the differentiation of indolent and metastatic tumors. Of course, these techniques can be used for any hyperpolarized ^{13}C molecules to study their in vivo distribution between different microenvironments.

Acknowledgments

The authors thank Dr. Duan Xu, Dr. Cornelius Von Morze, Dr. Ilwoo Park, Dr. Susan Noworolski, Mark Van Criekinge and Natalie Korn for helpful discussions and assistance performing experiments, and Dr. James Tropp for the custom ^{13}C coils. This work was supported by NIH grants R00 EB014328 (KRK), P41 EB013598 (DBV, JK), R01 CA166655 (JK) and R00 EB012064 (PEZL).

References

1. Padhani AR, Liu G, Koh DM, et al. Diffusion-weighted magnetic resonance imaging as a cancer biomarker: consensus and recommendations. 2009; 11:102–125. doi: 10.1593/neo.81328.
2. Sugahara T, Korogi Y, Kochi M, et al. Usefulness of diffusion-weighted MRI with echo-planar technique in the evaluation of cellularity in gliomas. J. Magn. Reson. Imaging. 1999; 9:53–60. [PubMed: 10030650]
3. Nagarajan R, Margolis D, Raman S, Sheng K, King C, Reiter R, Thomas MA. Correlation of Gleason Scores with Diffusion-Weighted Imaging Findings of Prostate Cancer. Advances in Urology. 2012; 2012:1–5. doi: 10.1002/jmri.20251.
4. Ardenkjær-Larsen J, Fridlund B, Gram A, Hansson G, Hansson L, Lerche M, Servin R, Thaning M, Golman K. Increase in signal-to-noise ratio of> 10,000 times in liquid-state NMR. Proc Natl Acad Sci USA. 2003; 100:10158. [PubMed: 12930897]
5. Keshari KR, Wilson DM. Chemistry and biochemistry of 13C hyperpolarized magnetic resonance using dynamic nuclear polarization. Chem. Soc. Rev. 2014; 43:1627. doi: 10.1039/c3cs60124b. [PubMed: 24363044]
6. Park I, Larson PEZ, Zierhut ML, et al. Hyperpolarized 13C magnetic resonance metabolic imaging: application to brain tumors. Neuro-oncology. 2010; 12:133–144. doi: 10.1093/neuonc/nop043. [PubMed: 20150380]
7. Albers M, Bok R, Chen A, Cunningham C, Zierhut M, Zhang V, Kohler S, Tropp J, Hurd R, Yen Y. Hyperpolarized 13C lactate, pyruvate, and alanine: noninvasive biomarkers for prostate cancer detection and grading. Cancer Research. 2008; 68:8607. [PubMed: 18922937]
8. Warburg O. On the origin of cancer cells. Science. 1956; 123:309–314. [PubMed: 13298683]
9. Nelson SJ, Kurhanewicz J, Vigneron DB, et al. Metabolic imaging of patients with prostate cancer using hyperpolarized [1-^{13}C]pyruvate. Sci Transl Med. 2013; 5:198ra108. doi: 10.1126/scitranslmed.3006070.
10. Gatenby R, Gillies R. Why do cancers have high aerobic glycolysis? Nat Rev Cancer. 2004; 4:891–899. [PubMed: 15516961]
11. Halestrap AP, Price NT. The proton-linked monocarboxylate transporter (MCT) family: structure, function and regulation. Biochem J. 1999; 343(Pt 2):281–299. [PubMed: 10510291]
12. Keshari KR, Sriram R, Koelsch BL, Van Criekinge M, Wilson DM, Kurhanewicz J, Wang ZJ. Hyperpolarized 13C-pyruvate magnetic resonance reveals rapid lactate export in metastatic renal

cell carcinomas. Cancer Research. 2013; 73:529–538. doi: 10.1158/0008-5472.CAN-12-3461. [PubMed: 23204238]

13. Koelsch BL, Keshari KR, Peeters TH, Larson PEZ, Wilson DM, Kurhanewicz J. Diffusion MR of hyperpolarized 13C molecules in solution. Analyst. 2013; 138:1011. doi: 10.1039/c2an36715g. [PubMed: 23304699]
14. Schilling F, Düwel S, Köllisch U, Durst M, Schulte RF, Glaser SJ, Haase A, Otto AM, Menzel MI. Diffusion of hyperpolarized (13) C-metabolites in tumor cell spheroids using real-time NMR spectroscopy. NMR in Biomedicine. 2013; 26:557–568. doi: 10.1002/nbm.2892. [PubMed: 23233311]
15. Koelsch, BL.; Keshari, KR.; Peeters, TH.; Larson, PEZ.; Wilson, DM.; Kurhanewicz, J. Complete Separation of Extra- and Intracellular Hyperpolarized 13C Metabolite Signal with Diffusion Weighted MR.. Proceedings of the 21st Annual Meeting of ISMRM; Salt Lake City, Utah, USA. 2013; p. 567
16. Larson PEZ, Kerr AB, Reed GD, Hurd RE, Kurhanewicz J, Pauly JM, Vigneron DB. Generating super stimulated-echoes in MRI and their application to hyperpolarized C-13 diffusion metabolic imaging. IEEE Trans Med Imaging. 2012; 31:265–275. doi: 10.1109/TMI.2011.2168235. [PubMed: 22027366]
17. Kettunen MI, Kennedy BWC, Hu D-E, Brindle KM. Spin echo measurements of the extravasation and tumor cell uptake of hyperpolarized [1-(13) C]lactate and [1-(13) C]pyruvate. Magn. Reson. Med. 2013; 70:1200–1209. doi: 10.1002/mrm.24591. [PubMed: 23280500]
18. Sogaard LV, Schilling F, Janich MA, Menzel MI, Ardenkjaer-Larsen JH. In vivomeasurement of apparent diffusion coefficients of hyperpolarized 13C-labeled metabolites. NMR in Biomedicine. 2014:n/a–n/a. doi: 10.1002/nbm.3093.
19. Gordon, JW.; Niles, DJ.; Fain, SB. Improved Measures of Renal Pyruvate-to-Lactate Conversion using Diffusion Gradients.. Proceedings of the 21st Annual Meeting of ISMRM; Salt Lake City, Utah, USA. 2013; p. 653
20. Chen AP, Albers MJ, Cunningham CH, et al. Hyperpolarized C-13 spectroscopic imaging of the TRAMP mouse at 3T-initial experience. Magn. Reson. Med. 2007; 58:1099–1106. doi: 10.1002/mrm.21256. [PubMed: 17969006]
21. Ohliger MA, Larson PEZ, Bok RA, et al. Combined parallel and partial fourier MR reconstruction for accelerated 8-channel hyperpolarized carbon-13 in vivo magnetic resonance Spectroscopic imaging (MRSI). J. Magn. Reson. Imaging. 2013; 38:701–713. doi: 10.1002/jmri.23989. [PubMed: 23293097]
22. Morze von C, Bok RA, Reed GD, Ardenkjaer-Larsen JH, Kurhanewicz J, Vigneron DB. Simultaneous Multiagent Hyperpolarized 13C Perfusion Imaging. Magn. Reson. Med. 2013 doi: 10.1002/mrm.25071.
23. Mayer D, Yen Y-F, Josan S, Park JM, Pfefferbaum A, Hurd RE, Spielman DM. Application of hyperpolarized [1-13C]lactate for the in vivo investigation of cardiac metabolism. NMR in Biomedicine. 2012; 25:1119–1124. doi: 10.1002/nbm.2778. [PubMed: 22278751]
24. Josan S, Yen Y-F, Hurd R, Pfefferbaum A, Spielman D, Mayer D. Application of double spin echo spiral chemical shift imaging to rapid metabolic mapping of hyperpolarized [1–13C]-pyruvate. J Magn Reson. 2011; 209:332–336. doi: 10.1016/j.jmr.2011.01.010. [PubMed: 21316280]
25. Cunningham CH, Chen AP, Albers MJ, Kurhanewicz J, Hurd RE, Yen Y-F, Pauly JM, Nelson SJ, Vigneron DB. Double spin-echo sequence for rapid spectroscopic imaging of hyperpolarized 13C. J Magn Reson. 2007; 187:357–362. doi: 10.1016/j.jmr.2007.05.014. [PubMed: 17562376]
26. Meyer CH, Pauly JM, Macovski A, Nishimura DG. Simultaneous spatial and spectral selective excitation. Magn. Reson. Med. 1990; 15:287–304. [PubMed: 2392053]
27. Lau AZ, Chen AP, Ghugre NR, Ramanan V, Lam WW, Connelly KA, Wright GA, Cunningham CH. Rapid multislice imaging of hyperpolarized 13C pyruvate and bicarbonate in the heart. Magn. Reson. Med. 2010; 64:1323–1331. doi: 10.1002/mrm.22525. [PubMed: 20574989]
28. Schulte RF, Sperl JI, Weidl E, et al. Saturation-recovery metabolic-exchange rate imaging with hyperpolarized [1-13C] pyruvate using spectral-spatial excitation. Magn. Reson. Med. 2013; 69:1209–1216. doi: 10.1002/mrm.24353. [PubMed: 22648928]

29. Park J-Y, DelaBarre L, Garwood M. Improved gradient-echo 3D magnetic resonance imaging using pseudo-echoes created by frequency-swept pulses. Magn. Reson. Med. 2006; 55:848–857. doi: 10.1002/mrm.20821. [PubMed: 16506188]
30. Hu, S.; Larson, PEZ.; Kerr, AB.; Kelly, DA.; Tropp, J.; Pauly, JM.; Kurhanewicz, J.; Vigneron, DB. Application of HSn Low Peak B1 Adiabatic Refocusing Pulse to Hyperpolarized 13C Spectoscopic Imaging.. Proceedings of the 17th Annual Meeting of ISMRM; Honolulu, Hawaii, USA. 2009; p. 333
31. Reese TG, Heid O, Weisskoff RM, Wedeen VJ. Reduction of eddy-current-induced distortion in diffusion MRI using a twice-refocused spin echo. Magn. Reson. Med. 2003; 49:177–182. doi: 10.1002/mrm.10308. [PubMed: 12509835]
32. Zhao L, Mulkern R, Tseng C, Williamson D, Patz S, Kraft R, Walsworth R, Jolesz F, Albert M. Gradient-Echo Imaging Considerations for Hyperpolarized 129Xe MR. J Magn Reson B. 1996; 113:179–183.
33. Nagashima K. Optimum pulse flip angles for multi-scan acquisition of hyperpolarized NMR and MRI. J Magn Reson. 2008; 190:183–188. doi: 10.1016/j.jmr.2007.10.011. [PubMed: 18023219]
34. Chaumeil MM, Larson PEZ, Yoshihara HAI, Danforth OM, Vigneron DB, Nelson SJ, Pieper RO, Phillips JJ, Ronen SM. Non-invasive in vivo assessment of IDH1 mutational status in glioma. Nat Commun. 2013; 4:2429. doi: 10.1038/ncomms3429. [PubMed: 24019001]
35. Bernstein, MA.; King, KF.; Zhou, XJ. Handbook of MRI Pulse Sequences. Elsevier Science; 2004.
36. Insko EK, Bolinger L. Mapping of the Radiofrequency Field. Journal of Magnetic Resonance Series A. 1993; 103:82–85.
37. Kono K, Inoue Y, Nakayama K, Shakudo M, Morino M, Ohata K, Wakasa K, Yamada R. The role of diffusion-weighted imaging in patients with brain tumors. AJNR Am J Neuroradiol. 2001; 22:1081–1088. [PubMed: 11415902]
38. Maier, SE.; Sun, Y.; Mulkern, RV. Diffusion imaging of brain tumors. In: Jensen, JH.; Helpern, JA., editors. NMR in Biomedicine. Vol. 23. 2010. p. 849-864.doi: 10.1002/nbm.1544
39. Le Bihan D, Poupon C, Amadon A, Lethimonnier F. Artifacts and pitfalls in diffusion MRI. J. Magn. Reson. Imaging. 2006; 24:478–488. doi: 10.1002/jmri.20683. [PubMed: 16897692]
40. Yen Y-F, Le Roux P, Mayer D, King R, Spielman D, Tropp J, Butts Pauly K, Pfefferbaum A, Vasanawala S, Hurd R. T 2relaxation times of 13C metabolites in a rat hepatocellular carcinoma model measured in vivousing 13C-MRS of hyperpolarized [1- 13C]pyruvate. NMR in Biomedicine. 2010:n/a–n/a. doi: 10.1002/nbm.1481.
41. Reed G, Morze von C, Bok R, Koelsch B, Van Criekinge M, Smith K, Shang H, Larson P, Kurhanewicz J, Vigneron D. High Resolution C-13 MRI With Hyperpolarized Urea: In Vivo T2 Mapping and N-15 Labeling Effects. IEEE Trans Med Imaging. 2014:22. doi: 10.1109/TMI.2013.2285120.
42. Fain SB, Korosec FR, Holmes JH, O'Halloran R, Sorkness RL, Grist TM. Functional lung imaging using hyperpolarized gas MRI. J. Magn. Reson. Imaging. 2007; 25:910–923. doi: 10.1002/jmri.20876. [PubMed: 17410561]
43. Chen XJ, Möller HE, Chawla MS, Cofer GP, Driehuys B, Hedlund LW, Johnson GA. Spatially resolved measurements of hyperpolarized gas properties in the lung in vivo. Part I: diffusion coefficient. Magn. Reson. Med. 1999; 42:721–728. [PubMed: 10502761]
44. Yablonskiy DA, Sukstanskii AL, Leawoods JC, Gierada DS, Bretthorst GL, Lefrak SS, Cooper JD, Conradi MS. Quantitative in vivo assessment of lung microstructure at the alveolar level with hyperpolarized 3He diffusion MRI. Proc Natl Acad Sci USA. 2002; 99:3111–3116. doi: 10.1073/pnas.052594699. [PubMed: 11867733]
45. Gerlinger M, Santos CR, Spencer-Dene B, et al. Genome-wide RNA interference analysis of renal carcinoma survival regulators identifies MCT4 as a Warburg effect metabolic target. J. Pathol. 2012; 227:146–156. doi: 10.1002/path.4006. [PubMed: 22362593]
46. Gallagher SM, Castorino JJ, Wang D, Philp NJ. Monocarboxylate transporter 4 regulates maturation and trafficking of CD147 to the plasma membrane in the metastatic breast cancer cell line MDA-MB-231. Cancer Research. 2007; 67:4182–4189. doi: 10.1158/0008-5472.CAN-06-3184. [PubMed: 17483329]

47. Stock C, Schwab A. Protons make tumor cells move like clockwork. Pflugers Arch. 2009; 458:981–992. doi: 10.1007/s00424-009-0677-8. [PubMed: 19437033]

48. Sotak CH. Multiple quantum NMR spectroscopy methods for measuring the apparent self-diffusion coefficient of in vivo lactic acid. NMR in Biomedicine. 1991; 4:70–72. [PubMed: 1859787]

49. Pfeuffer J, Lin JC, DelaBarre L, Uğurbil K, Garwood M. Detection of intracellular lactate with localized diffusion {1H–13C}-spectroscopy in rat glioma in vivo. J Magn Reson. 2005; 177:129–138. doi: 10.1016/j.jmr.2005.07.010. [PubMed: 16111904]

50. Koh DM, Takahara T, Imai Y, Collins DJ. Practical aspects of assessing tumors using clinical diffusion-weighted imaging in the body. Magn Reson Med Sci. 2007; 6:211–224. [PubMed: 18239358]

51. Clark CA, Le Bihan D. Water diffusion compartmentation and anisotropy at high b values in the human brain. Magn. Reson. Med. 2000; 44:852–859. [PubMed: 11108621]

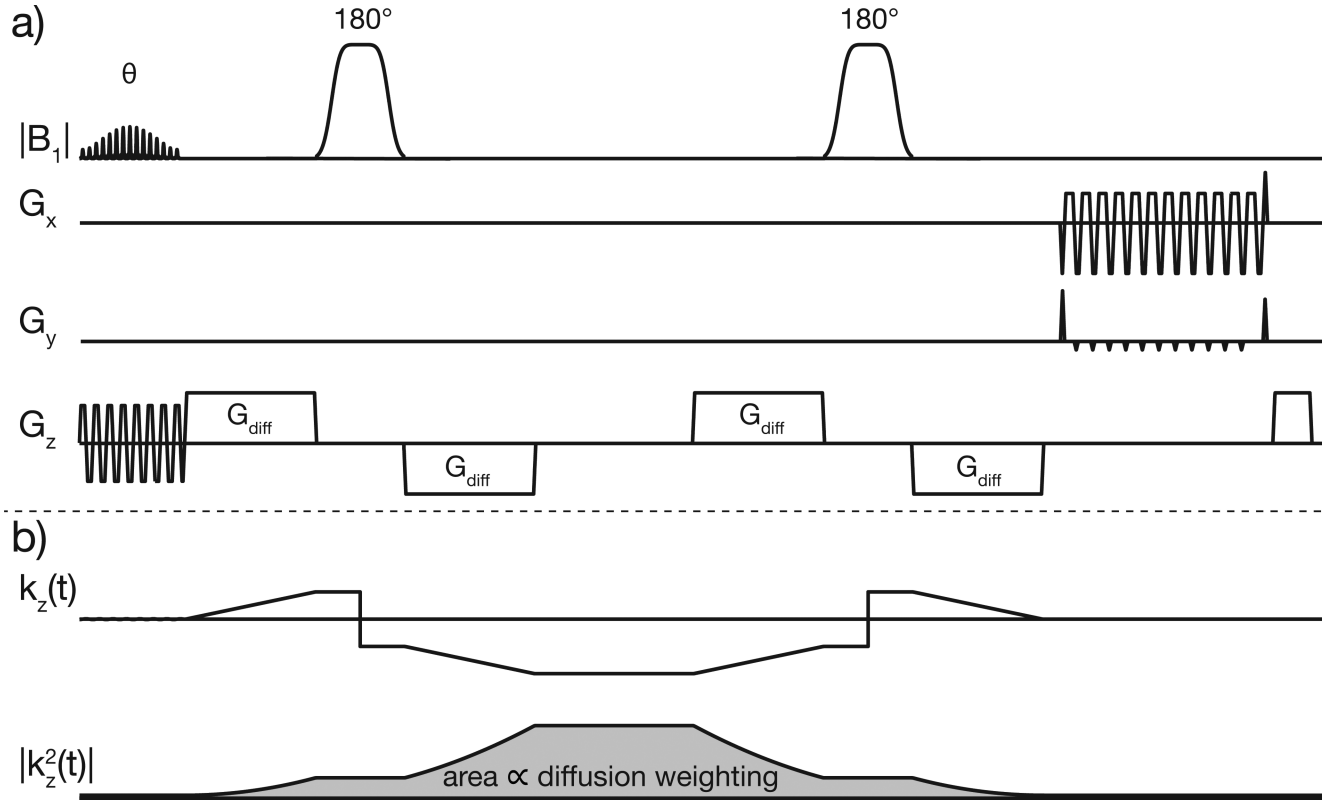

FIG 1.

(**a**) The bipolar pulsed-gradient double spin echo sequence used for diffusion weighting imaging of hyperpolarized ^{13}C metabolites on a clinical 3T MR scanner. The flip angle (θ) of the spectral-spatial excitation pulse is changed according to the variable flip angle (VFA) scheme. A single-shot echo-planar imaging (EPI) readout is followed by a crusher gradient. For these experiments, the slice-select and diffusion gradients were applied on G_z, while the EPI readout gradients were applied on the orthogonal axes. (**b**) The bipolar pulsed-gradients can apply diffusion weightings (*b*-values) upwards of 1,000 s mm^{-2} for ^{13}C, as represented by the shaded area under $|k^2_z(t)|$.

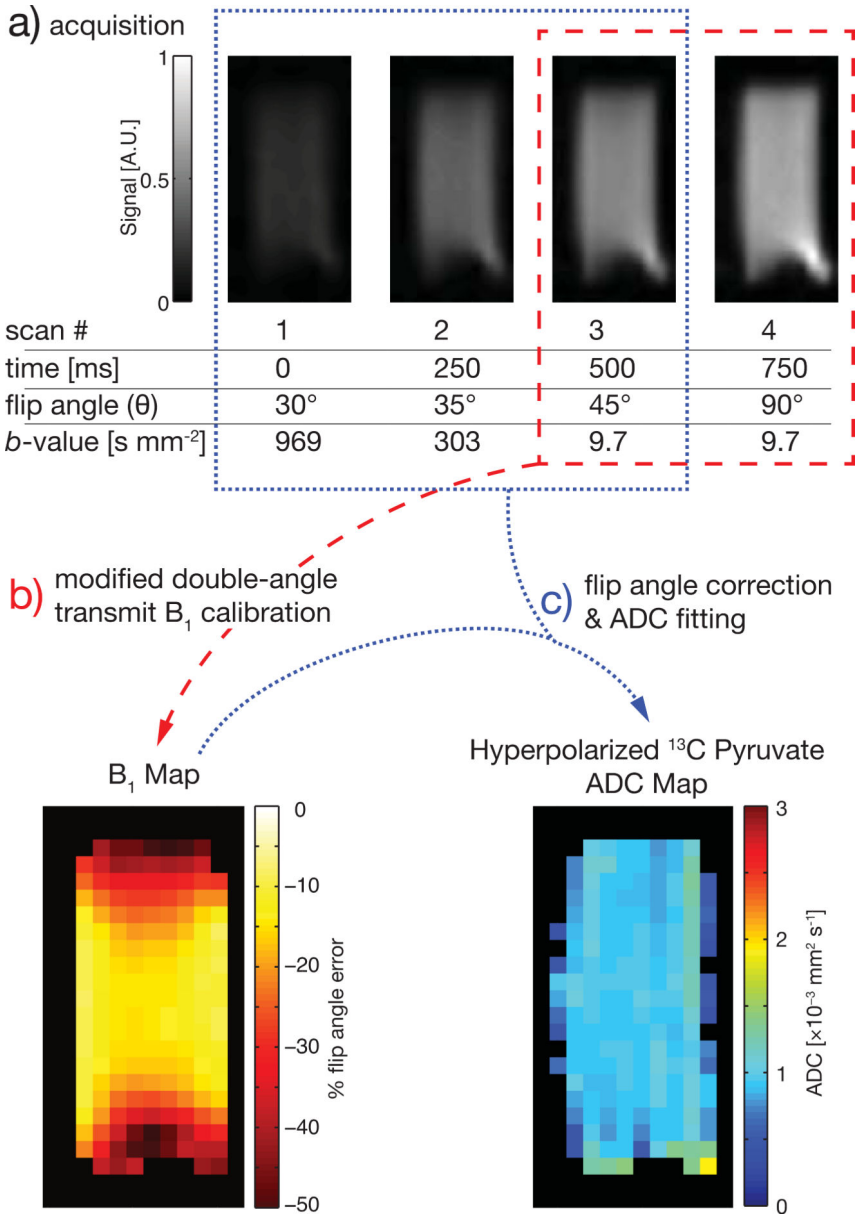

FIG 2.

A schematic of the methodology presented here for acquiring hyperpolarized ^{13}C metabolite diffusion weighted (DW) images and generating apparent diffusion coefficient (ADC) maps. The example data shown is a hyperpolarized ^{13}C pyruvate phantom at 22°C. **(a)** Each metabolite is scanned 4 times within 1 s with varying flip angles and *b*-values. **(b)** The SNR of the last 2 images are compared with a modified double angle method to produce a B_1 map. **(c)** The B_1 map is used for a voxel-wise flip angle correction of each image. ADC maps are calculated using the first 3 images.

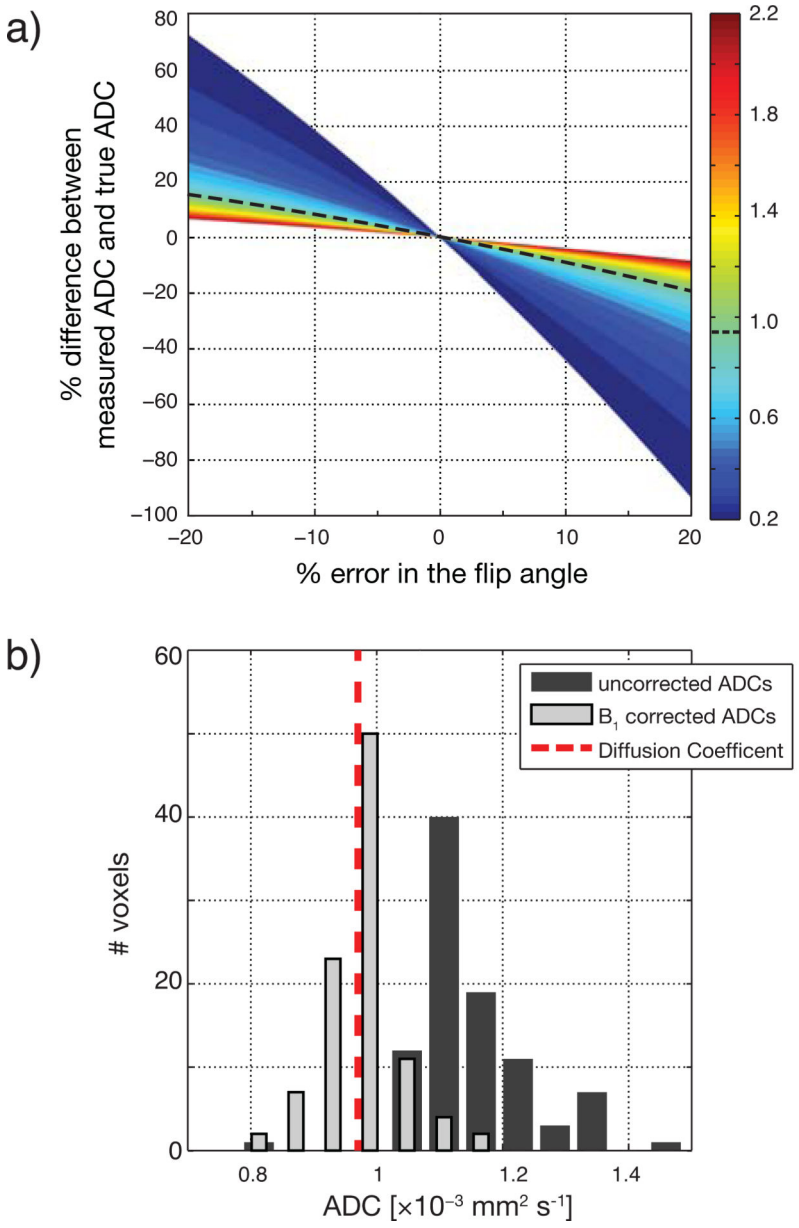

FIG 3.

Flip angle correction of the images based on the simultaneously acquired B_1 map improves ADC measurement accuracy. **(a)** This simulation demonstrates the effect that flip angle errors have on measured ADC, using the parameters presented in Figure 2. The black dotted line represents the diffusion coefficient of pyruvate at 22°C. **(b)** The voxel-wise distribution of ADCs for the hyperpolarized ^{13}C pyruvate phantom presented in Figure 2, before (*dark gray*) and after (*light gray*) a flip angle correction based on the B_1 map. The mean ADC of the corrected data aligns with the diffusion coefficient for pyruvate (*dotted line*).

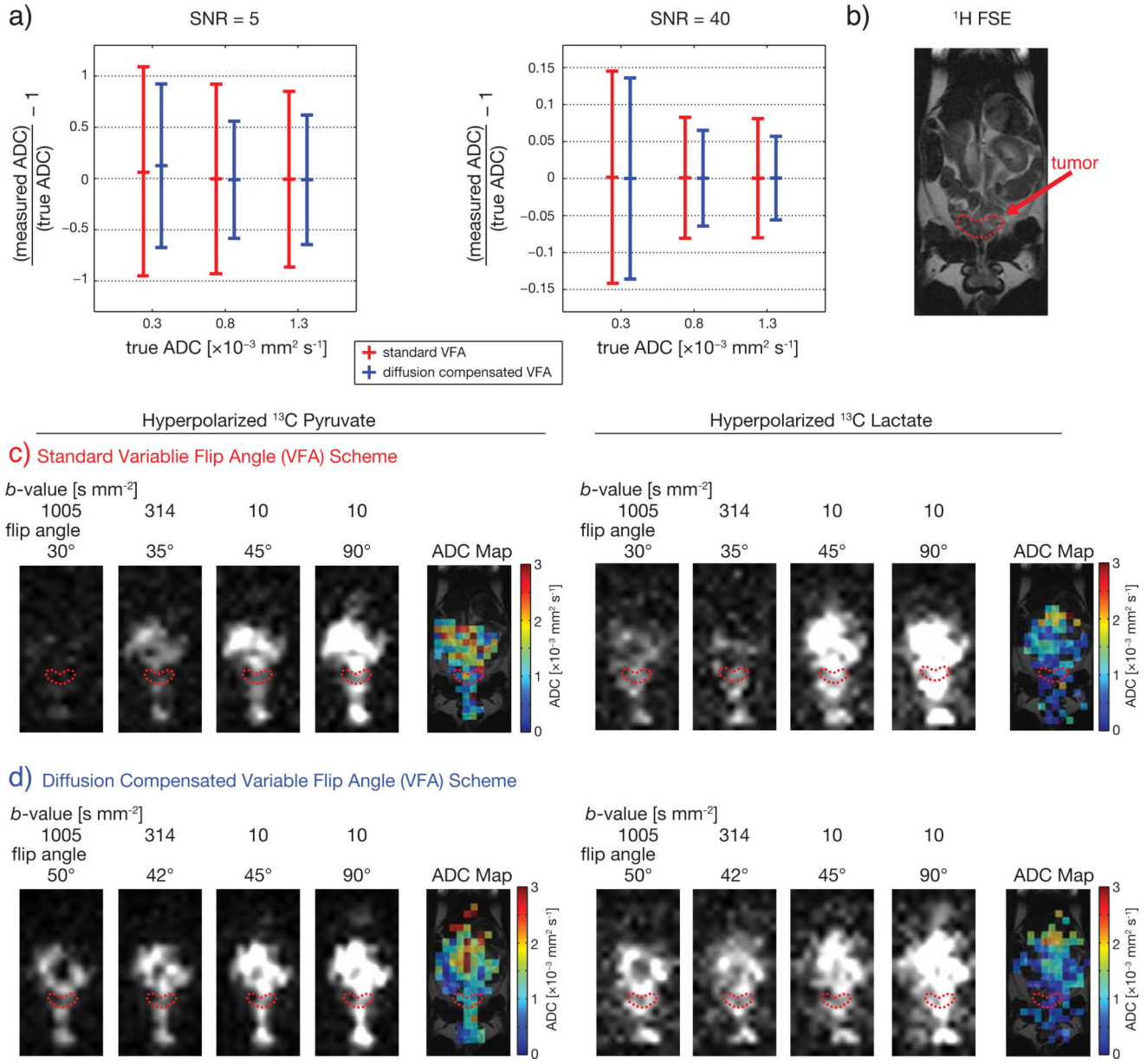

FIG 4.

Using a VFA scheme that compensates for SNR loss due to diffusion weighting leads to greater ADC measurement precision. **(a)** Simulated DW data demonstrates smaller standard deviations and improved ADC measurement precision achieved with the diffusion compensated VFA scheme (*blue*) rather than the standard VFA scheme (*red*), both with low (*left*) and high (*right*) SNR. **(b)** A TRAMP mouse with a small tumor. **(c)** The DW images acquired with the standard VFA for both hyperpolarized ^{13}C pyruvate and lactate show significantly decreased SNR at high *b*-values. **(d)** With the diffusion compensated VFA, the DW images of hyperpolarized ^{13}C pyruvate and lactate have significantly improved SNR at higher *b*-values, which improves the precision of ADC measurements. The DW images in (c) and (d) were windowed to the same SNR for each metabolite to illustrate the SNR differences between the two schemes.

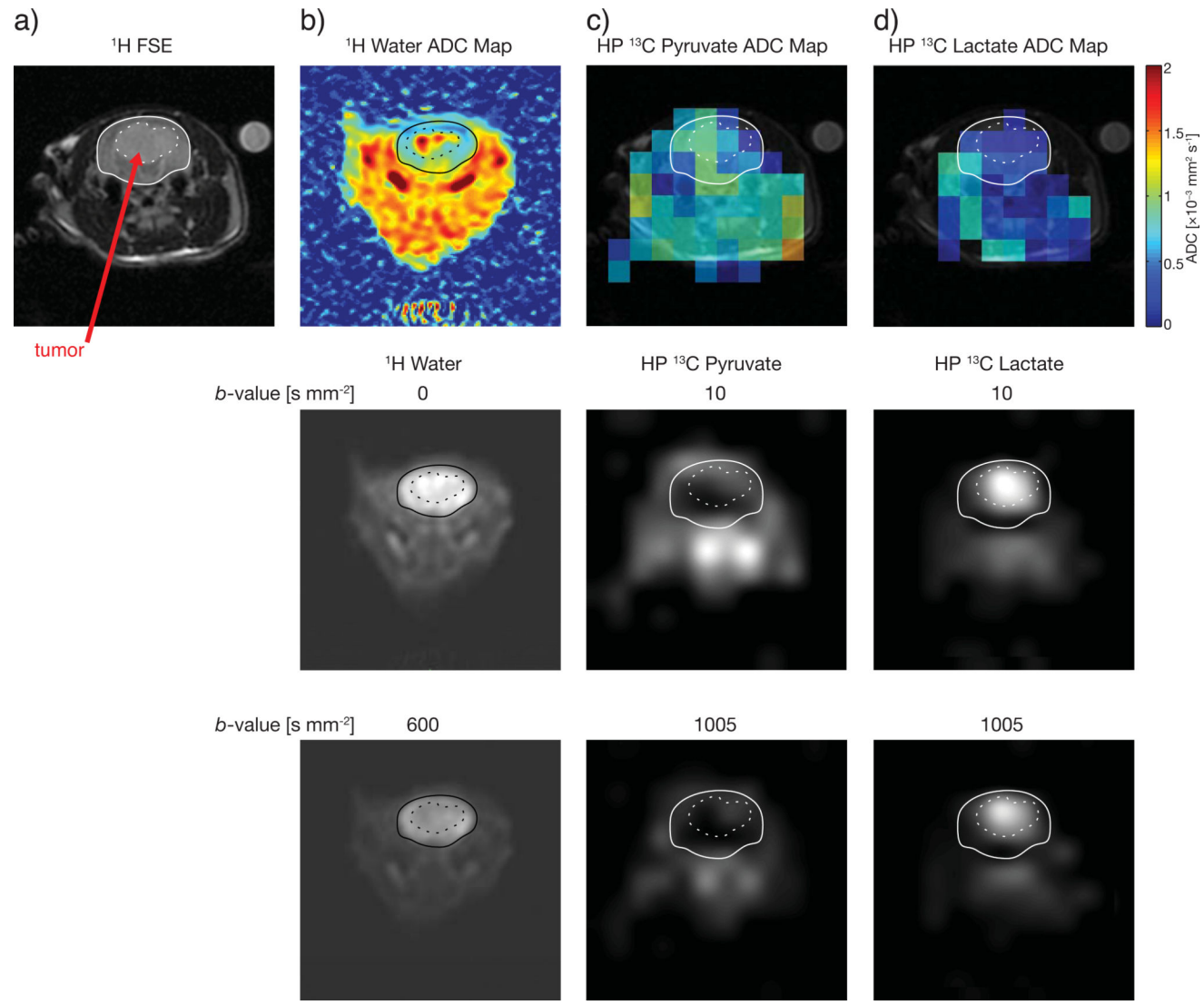

FIG 5.

The ADC maps for water and hyperpolarized ^{13}C pyruvate and lactate in a rat brain tumor model. **(a)** The proton FSE image with the brain (*solid line*) and the tumor (*dotted line*) outlined. **(b)** The water ADC map shows the tumor has an increased ADC relative to the surrounding normal brain tissue. Hyperpolarized ^{13}C images were acquired with the standard VFA scheme. **(c)** The hyperpolarized ^{13}C pyruvate ADC map showing relatively uniform ADCs across the normal brain and the tumor. **(d)** The ADC map of hyperpolarized ^{13}C lactate shows a decreased tumor ADC relative to the surrounding tissue. The corresponding low and high *b*-value DW images are shown below.

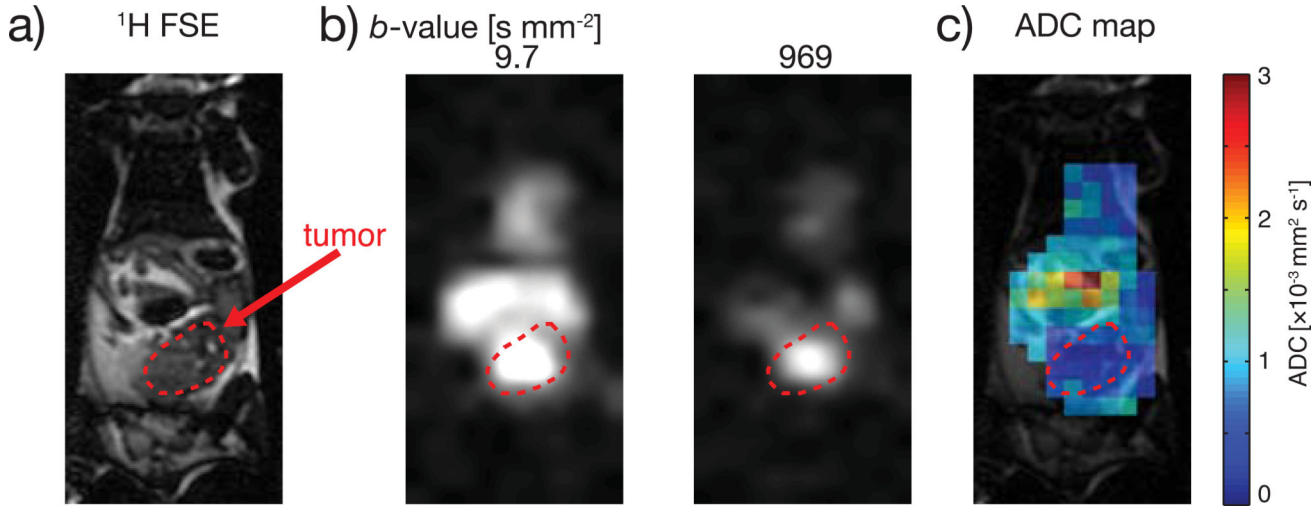

FIG 6.

The ADC map of hyperpolarized ^{13}C lactate prostate tumor bearing TRAMP mouse, acquired with the standard VFA scheme. **(a)** The proton FSE image with the tumor outlined. **(b)** The low and high *b*-value DW images of hyperpolarized ^{13}C lactate. Improved tumor contrast can be seen with a high *b*-value. **(c)** The ADC map clearly shows a decreased ADC in the tumor region in comparison to the surrounding tissue in the abdomen.

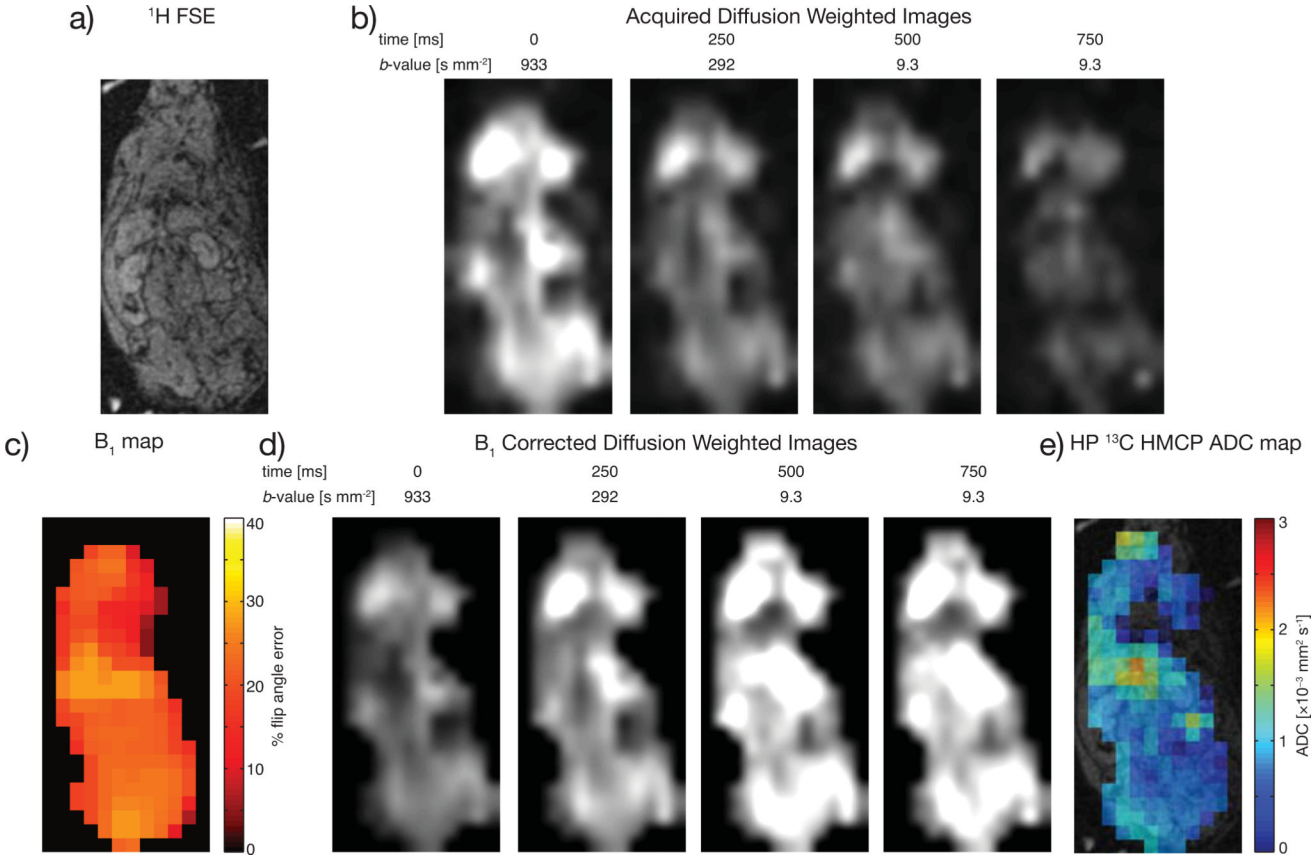

FIG 7.

ADC mapping of hyperpolarized ^{13}C HMCP in a normal rat using clinical trial-ready hardware. **(a)** The proton localizer image of the rat. **(b)** Having used a diffusion compensated VFA scheme and expecting constant SNR for all DW images, decreasing image SNR with decreasing *b*-values indicates that the transmitter power was too high. **(c)** The B_1 map reveals an average 22% ± 2 error in the flip angles and is use to correct the SNR in the DW images **(d)**. **(e)** The resulting ADC map shows a homogeneous ADC in the abdomen with increased ADCs seen at the descending aorta and portion of the intestine.